

UC Berkeley

UC Berkeley Previously Published Works

Title

Band Tailing and Deep Defect States in CH₃NH₃Pb(I_{1-x}Br_x)₃ Perovskites As Revealed by Sub-Bandgap Photocurrent

Permalink

<https://escholarship.org/uc/item/9bn2v70k>

Journal

ACS Energy Letters, 2(3)

ISSN

2380-8195

Authors

Sutter-Fella, Carolin M
Miller, D Westley
Ngo, Quynh P
[et al.](#)

Publication Date

2017-03-10

DOI

10.1021/acsenergylett.6b00727

Peer reviewed

This document is confidential and is proprietary to the American Chemical Society and its authors. Do not copy or disclose without written permission. If you have received this item in error, notify the sender and delete all copies.

Band Tailing and Deep Defect States in $\text{CH}_3\text{NH}_3\text{Pb}(\text{I}_{1-x}\text{Br}_x)_3$ Perovskites as Revealed by Sub-Bandgap Photocurrent

Journal:	ACS Energy Letters
Manuscript ID	nz-2016-00727w.R2
Manuscript Type:	Letter
Date Submitted by the Author:	n/a
Complete List of Authors:	<p>Sutter-Fella, Carolin; E O Lawrence Berkeley National Laboratory, Chemical Sciences Division; E O Lawrence Berkeley National Laboratory, Material Science Division; University of California Berkeley, Electrical Engineering and Computer Sciences Miller, D. Westley; Department of Physics Ngo, Quynh; University of California Berkeley, Electrical Engineering and Computer Sciences; E O Lawrence Berkeley National Laboratory, Materials Sciences Division Roe, Ellis; Department of Physics Toma, Francesca; E O Lawrence Berkeley National Laboratory, Chemical Sciences Division Sharp, Ian; Lawrence Berkeley National Laboratory, Chemical Sciences Division Lonergan, Mark; University of Oregon, Department of Chemistry and Biochemistry Javey, Ali; University of California, Berkeley, Dept. of Electrical Engineering/Comp Sci; University of California, Berkeley, Dept. of Electrical Engineering/Comp Sci</p>

SCHOLARONE™
Manuscripts

1
2
3
4
5
6
7
8
9
10
11
12
13
14
15
16
17
18
19
20
21
22
23
24
25
26
27
28
29
30
31
32
33
34
35
36
37
38
39
40
41
42
43
44
45
46
47
48
49
50
51
52
53
54
55
56
57
58
59
60

Band Tailing and Deep Defect States in $\text{CH}_3\text{NH}_3\text{Pb}(\text{I}_{1-x}\text{Br}_x)_3$ Perovskites as Revealed by Sub-Bandgap Photocurrent

Carolin M. Sutter-Fella^{†‡1}, D. Westley Miller^{#1}, Quynh P. Ngo^{†‡}, Ellis T. Roe[#],

Francesca M. Toma¹, Ian D. Sharp¹, Mark C. Lonergan^{&}, and Ali Javey^{†‡*}*

[†] Electrical Engineering and Computer Sciences, University of California, Berkeley, CA 94720,
United States

[‡] Materials Sciences Division, Lawrence Berkeley National Laboratory, Berkeley, CA 94720,
United States

¹ Chemical Sciences Division, Lawrence Berkeley National Laboratory, Berkeley, CA 94720,
United States

[#] Department of Physics, University of Oregon, Eugene, OR 97403, United States

[&] Department of Chemistry and Biochemistry, University of Oregon, Eugene, OR 97403,
United States

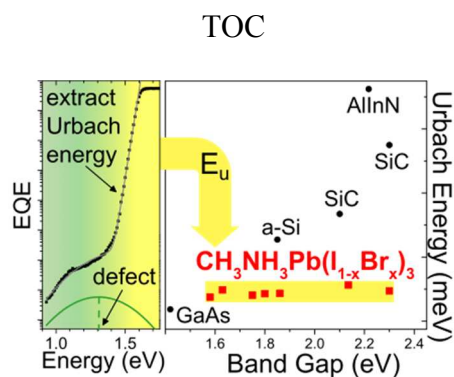
Corresponding Author

*E-mail Mark C. Lonergan: lonergan@uoregon.edu

*E-mail Ali Javey: ajavey@berkeley.edu

1
2
3
4
5
6
7
8
9
10
11
12
13
14
15
16
17
18
19
20
21
22
23
24
25
26
27
28
29
30
31
32
33
34
35
36
37
38
39
40
41
42
43
44
45
46
47
48
49
50
51
52
53
54
55
56
57
58
59
60

ABSTRACT Organometal halide perovskite semiconductors have emerged as promising candidates for optoelectronic applications because of the outstanding charge carrier transport properties, achieved with low temperature synthesis. Here, we present highly sensitive sub-bandgap external quantum efficiency (EQE) measurements of Au/spiro-OMeTAD/CH₃NH₃Pb(I_{1-x}Br_x)₃/TiO₂/FTO/glass photovoltaic devices. The room temperature spectra show exponential band tails with a sharp onset characterized by low Urbach energies (E_u) over the full halide composition space. The Urbach energies are 15 - 23 meV, lower than for most semiconductors with similar bandgaps (especially with $E_g > 1.9$ eV). Intentional aging of CH₃NH₃Pb(I_{1-x}Br_x)₃ for up to 2300 hours, reveals no change in E_u , despite the appearance of PbI₂ phase due to decomposition, and confirms a high degree of crystal ordering. Moreover, sub-bandgap EQE measurements reveal an extended band of sub-bandgap electronic states that can be fit with one or two point defects for pure CH₃NH₃PbI₃ or mixed CH₃NH₃Pb(I_{1-x}Br_x)₃ compositions, respectively. The study provides experimental evidence of defect states close to midgap that could impact photocarrier recombination and energy conversion efficiency in higher bandgap CH₃NH₃Pb(I_{1-x}Br_x)₃ alloys.



1
2
3
4
5
6 Organometal halide perovskites, with the general formula ABX_3 , have generated enormous
7
8 interest over the last 7 years as their solar cell power conversion efficiencies have increased from
9
10 3.8% in 2009¹ to the current world record of 22.1%². Much of this progress has been realized by
11
12 composition engineering, at the A site with cations³ including $CH(NH_2)_2^+$, $CH_3NH_3^+$, and Cs^+ , at
13
14 the B site with Pb^{2+} and Sn^{2+} cations⁴, and at the X site with I^- , Br^- , and Cl^- anions^{5,6}. These
15
16 changes have allowed researchers to increase photovoltaic power conversion efficiencies and
17
18 chemical stabilities, as well as engineer the band gap (E_g) for use in high efficiency tandem
19
20 photovoltaic devices.
21
22
23

24
25
26 Despite the intense interest in composition engineering, the effects of alloying on structural
27
28 disorder and the densities of states (DOS), particularly within the bandgap, are not well
29
30 documented. Their characterization is of central importance to identifying factors that contribute
31
32 to efficiency loss and instability for a number of reasons. First, defects cause non-radiative
33
34 recombination and modify the band alignment⁷, second, there is a growing consensus that
35
36 current-voltage hysteresis and photocurrent transients in organometal perovskite solar cells are
37
38 due to defect states and related mobile ionic species.^{7,8} Third, alloying might be expected to
39
40 increase disorder in a crystal as the variety of possible defect states is increased. Importantly, the
41
42 optical band edge, characterized by the Urbach energy (E_u)⁹, can be broadened by disorder in the
43
44 crystal lattice (or by impurities). Low Urbach energies are highly desirable for any
45
46 semiconductor used in optoelectronic devices. Finally, the evolution of defect states and
47
48 structural disorder upon aging could play a role in cell degradation.
49
50
51
52

53
54
55 Probing the role of defects and disorder on optoelectronic properties requires sensitive
56
57 spectroscopic probes. Defect transitions typically have much longer absorption lengths than
58
59
60

1
2
3 interband transitions therefore requiring the analysis of optical absorption over several orders of
4 magnitude below that at E_g . To this end, photothermal deflection spectroscopy (PDS)^{10,11} and
5 Fourier transform photocurrent spectroscopy (FTPS)¹⁰ have been performed on isolated thin
6 films, and sub-bandgap external quantum efficiency (EQE), transient photocapacitance, and
7 transient photocurrent measurements have been applied to full photovoltaic devices.^{12,13}
8
9

10 For $\text{CH}_3\text{NH}_3\text{PbI}_3$ films, previous PDS and FTPS measurements have shown a purely
11 exponential absorptance behavior with steep slopes that correspond to low values of E_u (~15
12 meV) and without the signatures of deep states within the band gap for up to four orders of
13 magnitude of response below E_g .¹⁰ Similarly low values of E_u have been observed for
14 $\text{CH}_3\text{NH}_3\text{PbBr}_3$ films by PDS (~25 meV)¹¹ and devices by photocurrent spectroscopy (~14
15 meV)¹⁴. Values on mixed bromide/iodide alloys $\text{CH}_3\text{NH}_3\text{Pb}(\text{I}_{1-x}\text{Br}_x)_3$ have been more varied.
16 Sadhanala et al. observed higher values of E_u at intermediate x with a peak of 90 meV for $x =$
17 0.8.¹¹ In contrast, Hoke et al. observed low values of $E_u = 12 - 17$ meV over nearly the full range
18 of x , with an outlier at $x = 0.5$.¹⁴
19
20
21
22
23
24
25
26
27
28
29
30
31
32
33
34
35
36
37

38 Although the methods described above have been successful at characterizing E_u in
39 $\text{CH}_3\text{NH}_3\text{Pb}(\text{I}_{1-x}\text{Br}_x)$ materials and solar cells, the signatures of electronically-active defect states
40 residing deep in the gap are rarely observed. In this regard, highly sensitive sub-bandgap EQE is
41 a particularly powerful approach because it is capable of probing ultra-low photocurrents due to
42 sub-bandgap absorption that can be several orders of magnitude weaker than absorption at E_g .
43 High sensitivity is enabled by using a high throughput monochromator, a low-noise current pre-
44 amplifier, and careful filtering of above bandgap stray light, allowing investigation of the sub-
45 bandgap DOS (see Supporting Information for experimental details). Indeed, this method has
46
47
48
49
50
51
52
53
54
55
56
57
58
59
60

1
2
3 recently been applied to $\text{CH}_3\text{NH}_3\text{PbI}_3$ solar cells to reveal a defect band at 1.34 eV with varying
4
5 density that was linked to photovoltaic characteristics.¹²
6
7

8
9 Here, we present sub-bandgap EQE measurements of $\text{Au/spiro-OMeTAD/CH}_3\text{NH}_3\text{Pb}(\text{I}_{1-x}\text{Br}_x)_3/\text{TiO}_2/\text{FTO/glass}$ photovoltaic devices at room temperature and extending over the full
10
11 halide composition space ($0 \leq x \leq 1$). In addition, we assess the impact of long-term aging of
12
13 devices under atmospheric conditions, as monitored via formation of PbI_2 , on photoluminescence
14
15 quantum yields and Urbach energies. Samples were aged for up to 2300 hours in a typical
16
17 laboratory environment with a temperature of 22 ± 1 ° C and a relative humidity of 50 ± 7 %. For
18
19 all compositions, we find Urbach energies in the range of 15 - 23 meV that remain
20
21 approximately constant throughout the experiment. Moreover, we find direct evidence of sub-
22
23 bandgap electronic states within the perovskite light absorbers. For pure $\text{CH}_3\text{NH}_3\text{PbI}_3$ a single,
24
25 relatively shallow state is observed. With increasing Br-content, this state moves closer to mid-
26
27 gap while another shallow defect is revealed. If the densities of the defect state nearest mid-gap
28
29 cannot be controlled, then they will likely enhance Shockley-Read-Hall recombination in higher
30
31 bandgap perovskites and potentially limit device performance. Our results provide important
32
33 insight into the defect characteristics of the explored perovskite compositions, with implications
34
35 for understanding disorder- and defect-induced performance limits.
36
37
38
39
40
41
42
43
44
45
46
47
48
49
50
51
52
53
54
55
56
57
58
59
60

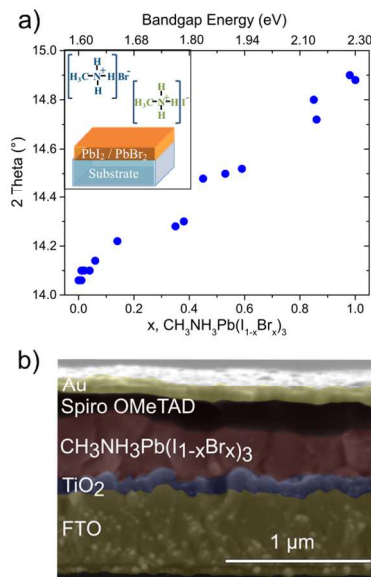


Figure 1. a) The change in the lattice parameter, as evaluated by the (110) X-ray diffraction peak angle, is plotted versus the halide composition, x , determined by EDX measurements. The methylammonium lead halide ($\text{CH}_3\text{NH}_3\text{Pb}(\text{I}_{1-x}\text{Br}_x)_3$) perovskite films were prepared by the vapor-assisted solution process (schematic inset). The upper x-axis provides the bandgap corresponding to composition, calculated according to Ref. 15. b) False colored cross-sectional scanning electron microscopy image of a typical planar $\text{Au}/\text{Spiro-OMeTAD}/\text{CH}_3\text{NH}_3\text{Pb}(\text{I}_{1-x}\text{Br}_x)_3/\text{TiO}_2/\text{FTO}$ photovoltaic device fabricated for this study.

$\text{CH}_3\text{NH}_3\text{Pb}(\text{I}_{1-x}\text{Br}_x)_3$ films on FTO/TiO_2 substrates were synthesized by a two-step, low-pressure, vapor-assisted, solution process (LP-VASP)^{15,16} that yields high material uniformity and quality, with previously reported solar cell power conversion efficiencies of up to 19%¹⁷. In brief, the process starts with spin-coating and drying of the $\text{PbI}_2/\text{PbBr}_2$ precursor on the substrate in a N_2 atmosphere for 15 minutes at 110 °C and is followed by annealing in $\text{CH}_3\text{NH}_3\text{I}$ and $\text{CH}_3\text{NH}_3\text{Br}$ vapor for two hours at 120 °C (schematic inset Figure 1a; details on device

1
2
3 processing can be found in the Supporting Information and Ref. 17). This process allows access
4
5 to the full halide composition space and results in the expected decrease of lattice parameter with
6
7 increasing Br content, as evaluated by the (110) X-ray diffraction peak angle. In Figure 1a, the
8
9 (110) peak angle is plotted versus the halide composition of the film, as measured by energy-
10
11 dispersive X-ray spectroscopy (7 kV, FEI Quanta FEG 250), and is approximately linear over
12
13 this small range of angles. The halide composition, x , in $\text{CH}_3\text{NH}_3\text{Pb}(\text{I}_{1-x}\text{Br}_x)_3$ was related to the
14
15 optical bandgap as described by the empirical equation $E_g(x) = 1.598 + 0.36x + 0.34x^2$ and is
16
17 displayed as the upper x-axis in Figure 1a.¹⁵ As mentioned above, sub-bandgap EQE
18
19 measurements were performed on photovoltaic devices. We fabricated the full stack of Au/spiro-
20
21 OMeTAD/ $\text{CH}_3\text{NH}_3\text{Pb}(\text{I}_{1-x}\text{Br}_x)_3/\text{TiO}_2/\text{FTO}/\text{glass}$ with a planar device architecture as illustrated in
22
23 the cross-sectional scanning electron microscopy image in Figure 1b.
24
25
26
27
28
29

30 The sub-bandgap EQE was measured using long-pass filters to limit above bandgap stray light
31
32 from a scanning monochromator to one part in 10^7 throughout most of the spectral range (more
33
34 experimental details can be found in the Supporting Information and in Ref. 12). Given that
35
36 light-induced halide segregation has been reported to create I- and Br-rich domains^{14,18}, it is
37
38 important to note that the monochromatic light intensity used during EQE measurements was $<$
39
40 $0.04 \text{ mW}/\text{cm}^2$ above the bandgap of all samples examined. The light intensity varied over the
41
42 spectral measurement and was below $0.4 \text{ mW}/\text{cm}^2$ at 0.8 eV, $0.04 \text{ mW}/\text{cm}^2$ at 1.6 eV, and 0.01
43
44 mW/cm^2 at 2.3 eV. This is much lower than the $10 - 100 \text{ mW}/\text{cm}^2$ used in the studies in which
45
46 varying degrees of light-induced halide segregation were observed.^{14,15,18} The proposed
47
48 mechanisms for halide segregation are predicated on the generation of mobile charges and ions,
49
50 thus low irradiances may limit halide segregation during the measurement. Furthermore,
51
52 according to prior work, halide segregation in these alloys is fully reversible within a few
53
54
55
56
57
58
59
60

minutes of relaxation in the dark.¹⁴ Because the EQE measurements reported here are performed at least 5 min after exposure to above bandgap light more intense than that used for the measurement itself and the sub-bandgap portion requires hours of data collection, the role of halide segregation should be limited. Nonetheless, light-induced halide segregation in mixed I/Br samples cannot be fully excluded and may contribute, in parallel to defect responses, to sub-bandgap absorption. However, transitions in the samples with $x = 0$ and 1, and below 1.59 eV cannot be explained by the formation of I-rich domains.

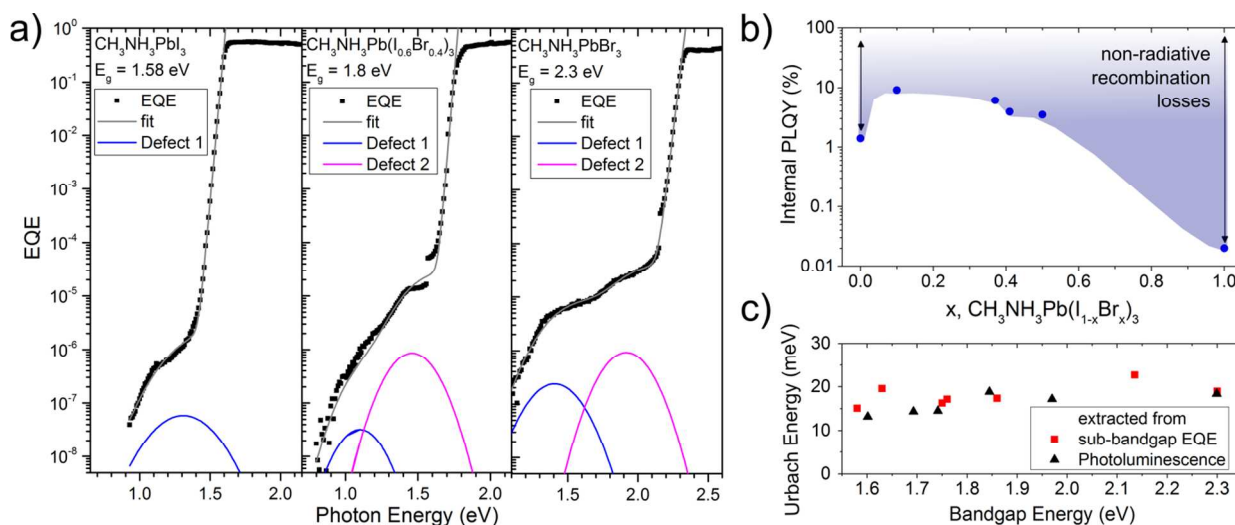


Figure 2. a) Sub-bandgap EQE spectra for $x = 0, 0.4,$ and 1 reveal the presence of electronically active defects. Fits to the data are shown as solid grey lines, with the underlying gaussian defect distributions shown as solid blue and magenta lines. b) Internal photoluminescence quantum yield (PLQY) extracted at 1-sun illumination for different $\text{CH}_3\text{NH}_3\text{Pb}(\text{I}_{1-x}\text{Br}_x)_3$ compositions. The shaded area illustrates non-radiative recombination losses. c) Summary of Urbach energies extracted from EQE and PL measurements plotted against the bandgap. The investigated

1
2
3 CH₃NH₃Pb(I_{1-x}Br_x)₃ films show consistently low Urbach energies between $15 \leq E_u \leq 23$ meV
4
5 over the full bandgap range of $1.6 \leq E_g \leq 2.3$ eV.
6
7
8
9

10
11
12 Representative sub-bandgap EQE spectra of CH₃NH₃Pb(I_{1-x}Br_x)₃ devices (with $x = 0, 0.4,$ and
13
14 1) are shown in Figure 2a together with the underlying gaussian defect distributions plotted as
15
16 solid blue and magenta lines (more sub-bandgap EQE spectra are illustrated in Figure S1 as well
17
18 as full EQE spectra on a linear scale in Figure S2, Supporting Information). They reveal
19
20 photocurrent due to optical transitions in the bandgap that likely involve point defects within the
21
22 perovskite thin films. Sub-bandgap defect-related transitions in the EQE spectra (EQE_d) were fit
23
24 using a function of the form:
25
26
27

$$EQE_d \propto 1 + \operatorname{erf}\left(\frac{E - E_d}{\sigma_d \sqrt{2}}\right)$$

28
29
30 where E_d is the optical transition energy of the defect, E is the incident photon energy, and σ_d
31
32 is the standard deviation of the underlying Gaussian energy density of states associated with a
33
34 point defect. This functional form is consistent with absorption due to a transition from a
35
36 Gaussian defect to the valence or conduction band and has been used to describe sub-bandgap
37
38 absorption spectra of many semiconductors (more information is given in the Supporting
39
40 Information)^{19,20}. For pure CH₃NH₃PbI₃, the best fit was obtained using a single defect model.
41
42 However, with increasing Br content, the bandgap opens and a second defect-related transition
43
44 emerges, requiring the use of a two-defect model to describe the response. All defect positions
45
46 given in the following are the optical transition energies with respect to a band edge, though the
47
48 technique does not provide information about the carrier type. The defect position (E_d) for the
49
50
51
52
53
54
55
56
57
58
59
60

1
2
3 sample with $x = 0$ was observed at 1.36 ± 0.06 eV. For the sample with $x = 0.4$, the two defects
4
5 were centered at 1.07 ± 0.06 eV and 1.43 ± 0.05 eV, and for the sample with $x = 1$, they were
6
7 located at 1.42 ± 0.03 eV and 1.89 ± 0.04 eV, respectively. Since the exceedingly low
8
9 photocurrents measured in sub-bandgap EQE could be generated in any part of the device,
10
11 reference measurements were performed on spiro-OMeTAD and TiO₂ photoconductors
12
13 (glass/FTO/spiro-OMeTAD/Au and glass/FTO/TiO₂/Ti, respectively) under identical conditions.
14
15 The spiro-OMeTAD photoconductor showed a weak sub-bandgap response centered at 2.2 eV
16
17 (see Supporting Information Figure S3), which is higher in energy than any defect response
18
19 observed from perovskite-containing photovoltaic devices. No sub-bandgap response was
20
21 observed from TiO₂. While the TiO₂ photoconductor would be expected to show a band-edge
22
23 optical response in the ultraviolet, the light source provided insufficient intensity in this spectral
24
25 range and did not produce any measurable photocurrent. Based on these reference measurements,
26
27 it is concluded that the sub-bandgap response detected from full photovoltaic device stacks is
28
29 generated within the CH₃NH₃Pb(I_{1-x}Br_x)₃ absorber layers. While the sub-bandgap EQE response
30
31 corresponds to transitions from bound to free electronic states that generate a photocurrent, it
32
33 does not indicate whether the observed transitions are associated with trapped holes that are
34
35 excited to the valence band or trapped electrons that are excited to the conduction band.
36
37 Therefore, further research will be required to identify the specific nature of these defects, as
38
39 well as their energetic positions on an absolute scale relative to each band edge, as a function of
40
41 composition. Regardless of the exact defect positions, the observed sub-bandgap responses
42
43 suggest that the higher bandgap alloys tend to form defects closer to mid-gap. For example, the
44
45 1.36 eV defect observed in the $x = 0$ sample corresponds to a state that is 220 meV from a band
46
47 edge, and 570 meV away from the midgap position. In stark contrast, the 1.42 eV transition seen
48
49
50
51
52
53
54
55
56
57
58
59
60

1
2
3 in the $x = 1$ sample is positioned 880 meV away from a band edge, and only 270 meV from the
4 middle of the bandgap. Defects closer to mid-gap are much more efficient recombination centers,
5 even for the same defect density.
6
7
8

9
10
11 In contrast to our finding, some previous density functional theory (DFT) studies have found
12 that deep defects should have prohibitively high formation energies in organolead iodide
13 perovskites.^{21,22} However, others predict a high density of deep traps under I-rich synthesis
14 conditions due to the formation of I-on-Pb antisite (I_{Pb}) defects with a formation energy < 0.2
15 eV.²³ The 1.36, 1.43 and 1.42 eV transitions observed in the $x = 0, 0.4$ and 1 cells, respectively
16 are within one standard deviation of each other and are a reasonably close match for the V_{Pb} (1-
17 /2-) transition energy predicted as the dominant defect for $x = 0$.²¹ Furthermore, this matches a
18 previously observed defect in $x = 0$ perovskites grown by another technique and whose density
19 was correlated with steady state performance losses and large J-V hysteresis.¹² Our findings are
20 most consistent with the V_{Pb} appearing at near the same energy relative to the conduction band
21 across the samples studied. The 1.89 eV transition observed in the $x = 1$ cell is a close match for
22 the V_{Pb} (0/-1) transition, which is predicted to be obscured by the valence band in
23 $CH_3NH_3PbI_3$.²¹ Previous studies have indicated that alloying $CH_3NH_3PbI_3$ with Br mostly shifts
24 the energetic position of the valence band^{24,25}, suggesting that such defect states would become
25 optoelectronically active as the bandgap opens. Note that the jump in the data appearing near
26 1.55 eV (Figure 2a) is an artifact of the measurement, due to the addition of a long pass filter at
27 that energy eliminating the contribution of above-bandgap stray light. The impact of stray light
28 on our EQE spectra is discussed in great detail in the Supporting Information.
29
30
31
32
33
34
35
36
37
38
39
40
41
42
43
44
45
46
47
48
49
50
51
52

53
54
55 Both time-resolved photoluminescence (PL)²⁶ and PL quantum yield¹⁵ measurements
56 corroborate the sub-bandgap EQE detection of deep defects by showing that trap-assisted
57
58
59
60

1
2
3 recombination is the limiting mechanism at low illumination intensities, which are of relevance
4 to the current work. In particular, the former study explained the monoexponential decay
5 observed at low laser fluence by monomolecular (trap-assisted) recombination and the latter
6 study suggested that trap-assisted recombination limits the PL quantum yield at illumination
7 intensities ≤ 1 sun for $0 \leq x \leq 1$. Figure 2b summarizes the internal PL quantum yield extracted at
8 1-sun illumination for different $\text{CH}_3\text{NH}_3\text{Pb}(\text{I}_{1-x}\text{Br}_x)_3$ compositions measured on LP-VASP
9 perovskite thin films. Further details on PL quantum yield measurements are reported in the
10 Supporting Information and have been published previously in Ref. 15. A PL quantum yield of
11 100 % would correspond to radiative recombination as the only recombination mechanism in the
12 studied sample. PL quantum yields below 100 % are indicative of non-radiative recombination
13 losses. Figure 2b indicates significantly lower quantum yield in $\text{CH}_3\text{NH}_3\text{PbBr}_3$. As we have
14 shown previously in our detailed PLQY analysis of $\text{CH}_3\text{NH}_3\text{Pb}(\text{I}_{1-x}\text{Br}_x)_3$ films, $\text{CH}_3\text{NH}_3\text{PbBr}_3$
15 seems to be limited by trap-assisted recombination over the full range of pump-powers used
16 (Ref. 15). Though, from PLQY it is not clear if the defect density is higher or if the depopulation
17 of traps is significantly faster for $x = 1$. The combination of PL quantum yield measurements
18 (which probe inherent film properties) indicating trap-assisted recombination at low illumination
19 intensities in the perovskite films (compare Supporting Information, Figure S4, and Ref. 15), and
20 sub-bandgap EQE data, revealing the presence of deep defect states in the absorber layer (with
21 increasing x) of active devices, suggests that deep defects could play an active role in affecting
22 performance characteristics of optoelectronic devices incorporating $\text{CH}_3\text{NH}_3\text{Pb}(\text{I}_{1-x}\text{Br}_x)_3$.
23
24
25
26
27
28
29
30
31
32
33
34
35
36
37
38
39
40
41
42
43
44
45
46
47
48
49
50

51 The Urbach energies extracted from EQE measurements versus bandgap are provided in
52 Figure 2c. Bandgaps were determined from Tauc plots²⁷ (further experimental details are
53 described in the Supporting Information), resulting in values in the expected range of 1.58 to 2.3
54
55
56
57
58
59
60

1
2
3 eV. Here, we also report the Urbach energies of LP-VASP samples grown on glass substrates
4
5 extracted from PL spectra using the van Roosbroeck-Shockley equation, where the optical
6
7 emission rate is related to the absorption coefficient.²⁸ All EQE spectra display sharp absorption
8
9 edges below E_g that translate into low Urbach energies (15 - 23 meV) and are in excellent
10
11 agreement with those obtained from PL spectra (13 - 19 meV).
12
13
14
15

16
17 It is interesting to compare Urbach energies of $\text{CH}_3\text{NH}_3\text{Pb}(\text{I}_{1-x}\text{Br}_x)_3$ films to a range of
18
19 technologically important inorganic semiconductors used in photovoltaic and other
20
21 optoelectronic applications. The Urbach energies obtained in this study from fitting of sub-
22
23 bandgap EQE data are plotted against their optical bandgaps, together with available literature
24
25 values, in Figure 3. The bandgap range accessible with $\text{CH}_3\text{NH}_3\text{Pb}(\text{I}_{1-x}\text{Br}_x)_3$ is highlighted ($1.6 \leq$
26
27 $E_g \leq 2.3$ eV) and clearly shows near constant Urbach energies that are significantly lower than in
28
29 conventional semiconductors, especially for $E_g > 1.9$ eV. This is remarkable given the
30
31 polycrystalline nature of the hybrid organic-inorganic perovskite thin films, and the nature of the
32
33 synthesis process, which does not exceed 120 °C and is performed on non-lattice matched
34
35 substrates. Furthermore, the available literature data for Urbach energies in $\text{CH}_3\text{NH}_3\text{Pb}(\text{I}_{1-x}\text{Br}_x)_3$
36
37 yielded significantly higher Urbach energy values than reported here for some of the mixed I/Br
38
39 compositions (compare blue triangles in Figure 3).^{11,14} Possibly, the synthesis method could play
40
41 a role in defining disorder, particularly in compositionally complex mixed halide perovskites.
42
43
44
45
46
47
48
49
50
51
52
53
54
55
56
57
58
59
60

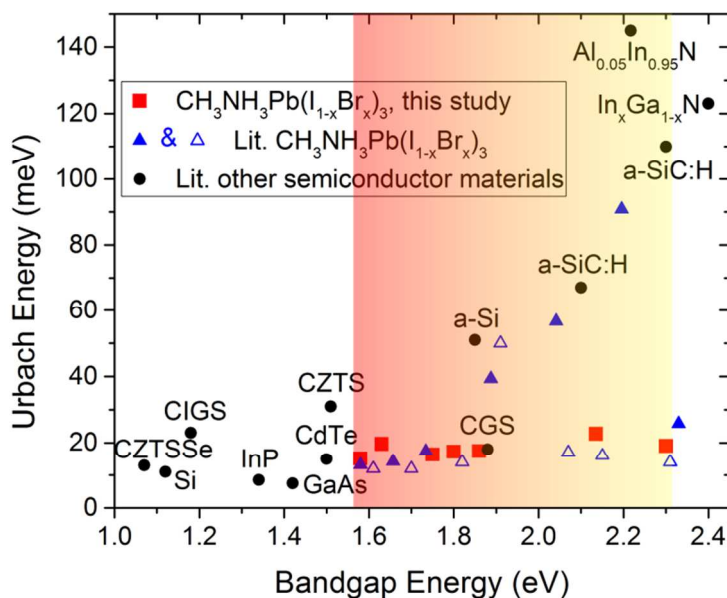


Figure 3. Urbach energies versus bandgap with the range accessible by $\text{CH}_3\text{NH}_3\text{Pb}(\text{I}_{1-x}\text{Br}_x)_3$ perovskites highlighted in the shaded region. Urbach energies from $\text{CH}_3\text{NH}_3\text{Pb}(\text{I}_{1-x}\text{Br}_x)_3$ perovskites in this study are shown as red squares and from literature data are shown as blue triangles^{11,14}. Also shown are a range of technologically important semiconductors (black dots): CZTSSe (Se-rich $\text{Cu}_2\text{ZnSn}(\text{S},\text{Se})_4$)²⁰, Si¹⁰, CIGS ($\text{Cu}(\text{In},\text{Ga})\text{Se}_2$)¹⁹, InP²⁹, GaAs³⁰, CdTe³¹, CZTS (S-rich $\text{Cu}_2\text{ZnSnS}_4$)²⁰, CGS (CuGaSe_2)³², a-Si³³, a-SiC:H³⁴, $\text{Al}_{0.05}\text{In}_{0.95}\text{N}$ ³⁵, $\text{In}_x\text{Ga}_{1-x}\text{N}$ (In-rich, graded In profile)³⁶.

While it is well established that methylammonium lead halide perovskites decompose upon exposure to ambient air³⁷, less is known about how this process impacts defects and disorder in the material. As mentioned earlier, the unencapsulated devices in this study were aged in the dark under laboratory conditions for up to 2300 h. Reaction with atmospheric species leaves PbI_2 as a primary solid state product. Therefore, X-ray diffraction (XRD) can be used to probe changes of the film in fully assembled devices, with the evolution of the (001) PbI_2 /(110)

1
2
3
4
5
6
7
8
9
10
11
12
13
14
15
16
17
18
19
20
21
22
23
24
25
26
27
28
29
30
31
32
33
34
35
36
37
38
39
40
41
42
43
44
45
46
47
48
49
50
51
52
53
54
55
56
57
58
59
60

perovskite (PbBr_2 /perovskite for $x = 1$) XRD integrated peak area ratio providing a useful metric for tracking decomposition as a function of time after synthesis. As shown in Figure 4a (and Figure S5a, Supporting Information), XRD reveals a general trend of increasing PbI_2 with time for mixed I/Br compositions, while the pure I- and Br-perovskite exhibit very little decomposition during the investigated time interval. In parallel, we recorded the sub-bandgap EQE data on the aged samples and extracted the Urbach energies. Figure 4b displays the evolution of the Urbach energies over time for different $\text{CH}_3\text{NH}_3\text{Pb}(\text{I}_{1-x}\text{Br}_x)_3$ devices. The data points are connected for better visibility and show approximately constant Urbach energies, in the range of 15 - 23 meV, for over 2300 h of degradation. This result indicates that aging and decomposition do not significantly increase disorder and band-tail states within the material.

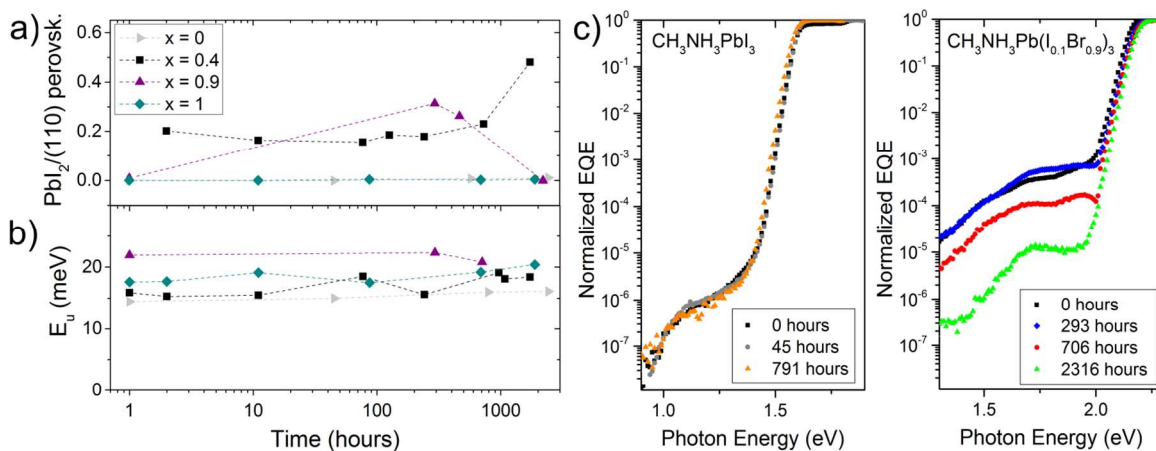


Figure 4. a) Repeated XRD measurements showing the integrated XRD peak ratio of (001) PbI_2 /(110) perovskite (PbBr_2 /perovskite for $x = 1$) phase as a function of time for different $\text{CH}_3\text{NH}_3\text{Pb}(\text{I}_{1-x}\text{Br}_x)_3$ compositions. b) Time evolution of Urbach energies under aging, as extracted from sub-bandgap EQE measurements. (data points in a and b are connected as a guide

1
2
3 for the eye) c) Sub-bandgap EQE spectra taken on the same photovoltaic devices as received (0
4
5
6 h) and after extended aging under laboratory conditions.
7
8
9

10
11
12 Examination of the EQE response further below the bandgap reveals that aging does not
13
14 increase concentrations of energetically deeper defect states, as shown in Figure 4c. For the case
15
16 of $\text{CH}_3\text{NH}_3\text{PbI}_3$ -based device, the defect-related response appears to be unaffected by aging for
17
18 up to 791 h, whereas for $\text{CH}_3\text{NH}_3\text{Pb}(\text{I}_{0.1}\text{Br}_{0.9})_3$ -based device the density of defect states seems to
19
20 decrease after 706 and 2316 hours of aging, during which time this mixed halide sample partially
21
22 decomposes, as indicated by the formation of PbI_2 . This finding is consistent with an observed
23
24 increase in internal PL quantum yield after several weeks of aging, which implies lower defect-
25
26 mediated recombination rates at low illumination intensities (Supporting Information S4). This
27
28 increase of PL efficiency with aging time can be explained by passivation of interface states by
29
30 formation of PbI_2 .^{38,39} After longer degradation times, it must be considered that the actual active
31
32 absorptive volume within the device is reduced due to consumption of the perovskite phase and
33
34 formation of PbI_2 , which leads to lower overall light absorption and, thus, lower photocurrent
35
36 response. It is also important to note that PbI_2 precipitation was highly non-uniform over the
37
38 sample (compare photograph in Figure S5b, Supporting Information) and XRD patterns
39
40 represent an average over regions much larger than the device area probed by EQE (*i.e.* XRD
41
42 samples regions with and without the Au contact layers, whereas EQE measurements only
43
44 sample the device active area under the Au contacts).
45
46
47
48
49
50
51
52

53 In summary, we have presented sub-bandgap EQE measurements on Au/spiro-
54
55 OMeTAD/ $\text{CH}_3\text{NH}_3\text{Pb}(\text{I}_{1-x}\text{Br}_x)_3/\text{TiO}_2/\text{FTO}/\text{glass}$ photovoltaic devices. All $\text{CH}_3\text{NH}_3\text{Pb}(\text{I}_{1-x}\text{Br}_x)_3$
56
57
58
59
60

1
2
3 compositions, with corresponding bandgaps of $1.6 \leq E_g \leq 2.3$ eV, exhibit low Urbach energies in
4
5 the range of 15 to 23 meV. These Urbach energies are significantly lower than most conventional
6
7 inorganic semiconductors with similar bandgaps, especially for $E_g > 1.9$ eV and are not affected
8
9 by long-term aging of perovskite-based photovoltaic devices (as indicated by co-presence of
10
11 PbI_2). Moreover, this study reveals the presence of sub-bandgap defect states for all
12
13 compositions. These states can be fit with one or two point defects for pure $\text{CH}_3\text{NH}_3\text{PbI}_3$ or
14
15 mixed $\text{CH}_3\text{NH}_3\text{Pb}(\text{I}_{1-x}\text{Br}_x)_3$ compositions, respectively. With increasing Br-content, the second
16
17 state emerges, and the observed defect responses indicate that the higher bandgap alloys are
18
19 characterized by deep level defects with states close to midgap. The combination of sub-bandgap
20
21 EQE, which can directly detect midgap states, and PL-based studies, which can identify
22
23 recombination pathways and probabilities, provides a future path toward assessing the roles of
24
25 synthesis and processing on efficiency-limiting recombination centers in the material.
26
27
28
29
30
31

32 ASSOCIATED CONTENT

33 **Supporting Information.**

34
35
36 The Supporting Information is available free of charge on the ACS Publications website.
37
38

39
40
41 Experimental section describing film formation, device processing, sensitive sub-bandgap EQE –
42
43 including fitting of the spectra, and PL quantum yield measurements. Sub-bandgap EQE
44
45 measurements on glass/FTO/spiro-OMeTAD/Au and glass/FTO/ TiO_2 /Ti photoconductors. Full
46
47 EQE spectra on a linear scale. PL quantum yield measurements on a $\text{CH}_3\text{NH}_3\text{Pb}(\text{I}_{0.9}\text{Br}_{0.1})_3$ film
48
49 under pump-power dependent illumination as-synthesized and re-measured after aging. XRD
50
51 measurements over time and photograph of aged sample.
52
53
54
55
56
57
58
59
60

1
2
3 AUTHOR INFORMATION
4
5

6 **Corresponding Author**
7

8
9 *E-mail Mark C. Lonergan: lonergan@uoregon.edu
10

11 *E-mail Ali Javey: ajavey@berkeley.edu
12
13

14 **Notes**
15

16
17 The authors declare no competing financial interest.
18
19

20 **Author Contributions**
21

22 The manuscript was written through contributions of all authors. All authors have given approval
23 to the final version of the manuscript. [†]These authors contributed equally.
24
25
26
27
28
29
30
31

32 **Acknowledgement**
33

34 Perovskite synthesis, characterization, and device fabrication were performed with support by
35 the Solar Photochemistry Program of the U.S. Department of Energy, Office of Science, Office
36 of Basic Energy Sciences, Division of Chemical, Geological and Biosciences under Contract No.
37 DE-AC02-05CH11231 (I.D.S.) and by the Laboratory Directed Research and Development
38 Program of Lawrence Berkeley National Laboratory under U.S. Department of Energy
39 contract number DE-AC02-05CH11231 (F.M.T). The optical characterization and quantum
40 yield measurements were supported by the Electronic Materials program, funded by the Director,
41 Office of Science, Office of Basic Energy Sciences, Materials Sciences and Engineering
42 Division of the U.S. Department of Energy under Contract No. DE-AC02-05CH11231. Some
43 electrical performance measurements were performed at the Molecular Foundry, which is
44
45
46
47
48
49
50
51
52
53
54
55
56
57
58
59
60

1
2
3 supported by the Office of Science, Office of Basic Energy Sciences, of the U.S. Department of
4 Energy under Contract No. DE-AC02-05CH11231. The sub-bandgap EQE measurements and
5 analyses presented were funded by the Office of Basic Energy Sciences of the U.S. Department
6 of Energy through DE-SC0012363. This work utilized equipment in the SuNRise Photovoltaic
7 Laboratory supported by Oregon BEST. C. M. S.-F. acknowledges financial support from the
8 Swiss National Science Foundation (P2EZIP2_155586).
9
10
11
12
13
14
15
16
17
18
19
20
21
22
23
24
25
26
27
28
29
30

31 REFERENCES

- 32
33
34 (1) Kojima, A.; Teshima, K.; Shirai, Y.; Miyasaka, T. Organometal Halide Perovskites as
35 Visible-Light Sensitizers for Photovoltaic Cells. *J. Am. Chem. Soc.* **2009**, *131*, 6050–6051.
36
37 (2) Zhang, W.; Eperon, G. E.; Snaith, H. J. Metal Halide Perovskites for Energy
38 Applications. *Nat. Energy* **2016**, *1*, 16048.
39
40 (3) Saliba, M.; Matsui, T.; Seo, J.-Y.; Domanski, K.; Correa-Baena, J.-P.; Nazeeruddin, M.
41 K.; Zakeeruddin, S. M.; Tress, W.; Abate, A.; Hagfeldt, A.; Grätzel, M. Cesium-Containing
42 Triple Cation Perovskite Solar Cells: Improved Stability, Reproducibility and High Efficiency.
43 *Energy Environ. Sci.* **2016**, *9*, 1989–1997.
44
45 (4) Eperon, G. E.; Leijtens, T.; Bush, K. A.; Green, T.; Wang, J. T.-W.; McMeekin, D. P.;
46 Volonakis, G.; Milot, R. L.; Slotcavage, D. J.; Belisle, R. et al. Perovskite-Perovskite Tandem
47 Photovoltaics with Ideal Bandgaps. *ArXiv160803920 Cond-Mat* **2016** (DOI:
48 10.1126/science.aaf9717).
49
50 (5) Noh, J. H.; Im, S. H.; Heo, J. H.; Mandal, T. N.; Seok, S. I. Chemical Management for
51 Colorful, Efficient, and Stable Inorganic–Organic Hybrid Nanostructured Solar Cells. *Nano Lett.*
52 **2013**, *13*, 1764–1769.
53
54 (6) Sadhanala, A.; Ahmad, S.; Zhao, B.; Giesbrecht, N.; Pearce, P. M.; Deschler, F.; Hoye,
55
56
57
58
59
60

1
2
3 R. L. Z.; Gödel, K. C.; Bein, T.; Docampo, P. et al. Blue-Green Color Tunable Solution
4 Processable Organolead Chloride–Bromide Mixed Halide Perovskites for Optoelectronic
5 Applications. *Nano Lett.* **2015**, *15*, 6095–6101.

6
7
8 (7) Ball, J. M.; Petrozza, A. Defects in Perovskite-Halides and Their Effects in Solar Cells.
9 *Nat. Energy* **2016**, *1*, 16149.

10
11 (8) Unger, E. L.; Hoke, E. T.; Bailie, C. D.; Nguyen, W. H.; Bowring, A. R.; Heumüller, T.;
12 Christoforo, M. G.; McGehee, M. D. Hysteresis and Transient Behavior in Current–voltage
13 Measurements of Hybrid-Perovskite Absorber Solar Cells. *Energy Environ. Sci.* **2014**, *7*, 3690–
14 3698.

15
16
17 (9) Urbach, F. The Long-Wavelength Edge of Photographic Sensitivity and of the Electronic
18 Absorption of Solids. *Phys. Rev.* **1953**, *92*, 1324–1324.

19
20 (10) De Wolf, S.; Holovsky, J.; Moon, S.-J.; Löper, P.; Niesen, B.; Ledinsky, M.; Haug, F.-J.;
21 Yum, J.-H.; Ballif, C. Organometallic Halide Perovskites: Sharp Optical Absorption Edge and Its
22 Relation to Photovoltaic Performance. *J. Phys. Chem. Lett.* **2014**, *5*, 1035–1039.

23
24 (11) Sadhanala, A.; Deschler, F.; Thomas, T. H.; Dutton, S. E.; Goedel, K. C.; Hanusch, F. C.;
25 Lai, M. L.; Steiner, U.; Bein, T.; Docampo, P. et al. Preparation of Single-Phase Films of
26 $\text{CH}_3\text{NH}_3\text{Pb}(\text{I}_{1-x}\text{Br}_x)_3$ with Sharp Optical Band Edges. *J. Phys. Chem. Lett.* **2014**, *5*, 2501–2505.

27
28
29 (12) Miller, D. W.; Eperon, G. E.; Roe, E. T.; Warren, C. W.; Snaith, H. J.; Lonergan, M. C.
30 Defect States in Perovskite Solar Cells Associated with Hysteresis and Performance. *Appl. Phys.*
31 *Lett.* **2016**, *109*, 153902.

32
33 (13) Wang, H.-P.; Sutter-Fella, C. M.; Lobaccaro, P.; Hettick, M.; Zheng, M.; Lien, D.-H.;
34 Miller, D. W.; Warren, C. W.; Roe, E. T.; Lonergan, M. C. et al. Increased Optoelectronic
35 Quality and Uniformity of Hydrogenated P-InP Thin Films. *Chem. Mater.* **2016**, *28*, 4602–4607.

36
37 (14) Hoke, E. T.; Slotcavage, D. J.; Dohner, E. R.; Bowring, A. R.; Karunadasa, H. I.;
38 McGehee, M. D. Reversible Photo-Induced Trap Formation in Mixed-Halide Hybrid Perovskites
39 for Photovoltaics. *Chem. Sci.* **2014**, *6*, 613–617.

40
41
42 (15) Sutter-Fella, C. M.; Li, Y.; Amani, M.; Ager, J. W.; Toma, F. M.; Yablonovitch, E.;
43 Sharp, I. D.; Javey, A. High Photoluminescence Quantum Yield in Band Gap Tunable Bromide
44 Containing Mixed Halide Perovskites. *Nano Lett.* **2016**, *16*, 800–806.

45
46 (16) Li, Y.; Cooper, J. K.; Buonsanti, R.; Giannini, C.; Liu, Y.; Toma, F. M.; Sharp, I. D.
47 Fabrication of Planar Heterojunction Perovskite Solar Cells by Controlled Low-Pressure Vapor
48 Annealing. *J. Phys. Chem. Lett.* **2015**, *6*, 493–499.

49
50
51 (17) Li, Y.; Cooper, J. K.; Liu, W.; Sutter-Fella, C. M.; Amani, M.; Beeman, J. W.; Javey, A.;
52 Ager, J. W.; Liu, Y.; Toma, F. M. et al. Defective TiO_2 with High Photoconductive Gain for
53 Efficient and Stable Planar Heterojunction Perovskite Solar Cells. *Nat. Commun.* **2016**, *7*, 12446.

54
55 (18) Bischak, C. G.; Hetherington, C. L.; Wu, H.; Aloni, S.; Ogletree, D. F.; Limmer, D. T.;
56 Ginsberg, N. S. Origin of Reversible Photo-Induced Phase Separation in Hybrid Perovskites.
57 *ArXiv160607366 Cond-Mat Physics* **2016**.

- 1
2
3 (19) Heath, J. T.; Cohen, J. D.; Shafarman, W. N.; Liao, D. X.; Rockett, A. A. Effect of Ga
4 Content on Defect States in $\text{CuIn}_{1-x}\text{Ga}_x\text{Se}_2$ Photovoltaic Devices. *Appl. Phys. Lett.* **2002**, *80*,
5 4540–4542.
6
7
8 (20) Miller, D. W.; Warren, C. W.; Gunawan, O.; Gokmen, T.; Mitzi, D. B.; Cohen, J. D.
9 Electronically Active Defects in the $\text{Cu}_2\text{ZnSn}(\text{Se,S})_4$ Alloys as Revealed by Transient
10 Photocapacitance Spectroscopy. *Appl. Phys. Lett.* **2012**, *101*, 142106.
11
12 (21) Yin, W.-J.; Shi, T.; Yan, Y. Unusual Defect Physics in $\text{CH}_3\text{NH}_3\text{PbI}_3$ Perovskite Solar
13 Cell Absorber. *Appl. Phys. Lett.* **2014**, *104*, 63903.
14
15 (22) Yin, W.-J.; Shi, T.; Yan, Y. Unique Properties of Halide Perovskites as Possible Origins
16 of the Superior Solar Cell Performance. *Adv. Mater.* **2014**, *26*, 4653–4658.
17
18 (23) Buin, A.; Pietsch, P.; Xu, J.; Voznyy, O.; Ip, A. H.; Comin, R.; Sargent, E. H. Materials
19 Processing Routes to Trap-Free Halide Perovskites. *Nano Lett.* **2014**, *14*, 6281–6286.
20
21 (24) Schulz, P.; Edri, E.; Kirmayer, S.; Hodes, G.; Cahen, D.; Kahn, A. Interface Energetics in
22 Organo-Metal Halide Perovskite-Based Photovoltaic Cells. *Energy Environ. Sci.* **2014**, *7*, 1377–
23 1381.
24
25 (25) Butler, K. T.; Frost, J. M.; Walsh, A. Band Alignment of the Hybrid Halide Perovskites
26 $\text{CH}_3\text{NH}_3\text{PbCl}_3$, $\text{CH}_3\text{NH}_3\text{PbBr}_3$ and $\text{CH}_3\text{NH}_3\text{PbI}_3$. *Mater. Horiz.* **2015**, *2*, 228–231.
27
28 (26) Stranks, S. D.; Burlakov, V. M.; Leijtens, T.; Ball, J. M.; Goriely, A.; Snaith, H. J.
29 Recombination Kinetics in Organic-Inorganic Perovskites: Excitons, Free Charge, and Subgap
30 States. *Phys. Rev. Appl.* **2014**, *2*, 34007.
31
32 (27) Tauc, J.; Grigorovici, R.; Vancu, A. Optical Properties and Electronic Structure of
33 Amorphous Germanium. *Phys. Status Solidi B* **1966**, *15*, 627–637.
34
35 (28) van Roosbroeck, W.; Shockley, W. Photon-Radiative Recombination of Electrons and
36 Holes in Germanium. *Phys. Rev.* **1954**, *94*, 1558–1560.
37
38 (29) Chen, K.; Kapadia, R.; Harker, A.; Desai, S.; Seuk Kang, J.; Chuang, S.; Tosun, M.;
39 Sutter-Fella, C. M.; Tsang, M.; Zeng, Y. et al. Direct Growth of Single-Crystalline III-V
40 Semiconductors on Amorphous Substrates. *Nat. Commun.* **2016**, *7*, 10502.
41
42 (30) Johnson, S. R.; Tiedje, T. Temperature Dependence of the Urbach Edge in GaAs. *J. Appl.*
43 *Phys.* **1995**, *78*, 5609–5613.
44
45 (31) Warren, C. W.; Li, J.; Wolden, C. A.; Meysing, D. M.; Barnes, T. M.; Miller, D. W.;
46 Heath, J. T.; Lonergan, M. C. The Effect of Copper on the Sub-Bandgap Density of States of
47 CdTe Solar Cells. *Appl. Phys. Lett.* **2015**, *106*, 203903.
48
49 (32) Cohen, J. D. *Identifying the Electronic Properties Relevant to Improving the*
50 *Performance of High Band-Gap Copper Based I-III-VI₂ Chalcopyrite Thin Film Photovoltaic*
51 *Devices*; Subcontract Report NREL/SR-520-43909; **2008**.
52
53 (33) Veen, M. K. van; Schropp, R. E. I. Beneficial Effect of a Low Deposition Temperature of
54
55
56
57
58
59
60

1
2
3 Hot-Wire Deposited Intrinsic Amorphous Silicon for Solar Cells. *J. Appl. Phys.* **2003**, *93*, 121–
4 125.

5
6
7 (34) Conde, J. P.; Chu, V.; Silva, M. F. da; Kling, A.; Dai, Z.; Soares, J. C.; Arekat, S.;
8 Fedorov, A.; Berberan-Santos, M. N.; Giorgis, F.; Pirri, C. F. Optoelectronic and Structural
9 Properties of Amorphous Silicon–carbon Alloys Deposited by Low-Power Electron-Cyclotron
10 Resonance Plasma-Enhanced Chemical-Vapor Deposition. *J. Appl. Phys.* **1999**, *85*, 3327–3338.

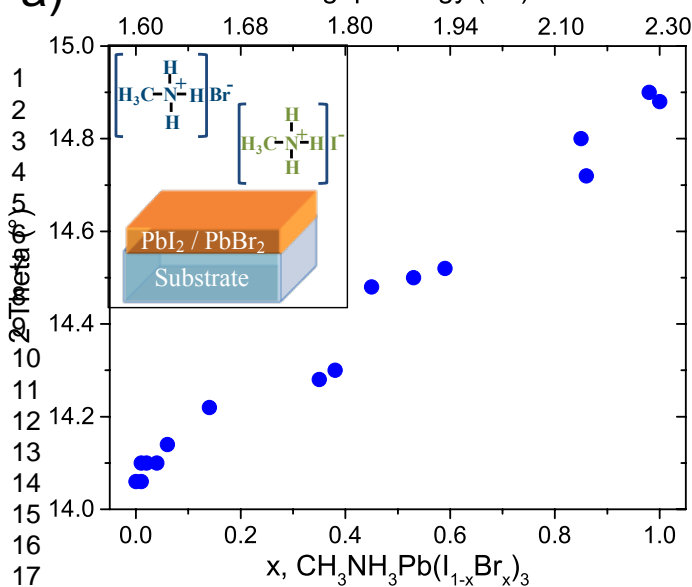
11
12 (35) Jiang, L. F.; Shen, W. Z.; Guo, Q. X. Temperature Dependence of the Optical Properties
13 of AlInN. *J. Appl. Phys.* **2009**, *106*, 13515.

14
15 (36) Valdueza-Felip, S.; Bellet-Amalric, E.; Núñez-Cascajero, A.; Wang, Y.; Chauvat, M.-P.;
16 Ruterana, P.; Pouget, S.; Lorenz, K.; Alves, E.; Monroy, E. High In-Content InGaN Layers
17 Synthesized by Plasma-Assisted Molecular-Beam Epitaxy: Growth Conditions, Strain
18 Relaxation, and In Incorporation Kinetics. *J. Appl. Phys.* **2014**, *116*, 233504.

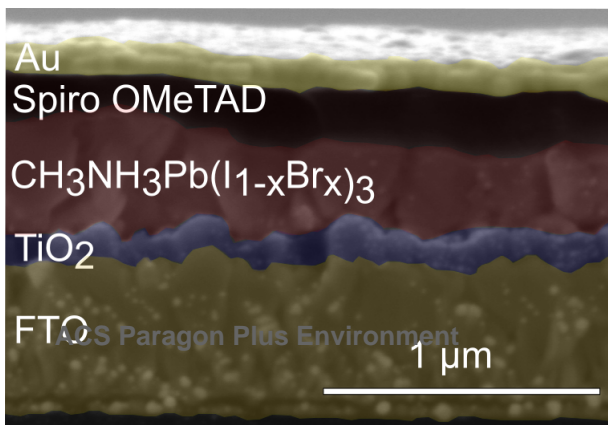
19
20 (37) Tiep, N. H.; Ku, Z.; Fan, H. J. Recent Advances in Improving the Stability of Perovskite
21 Solar Cells. *Adv. Energy Mater.* **2016**, *6*, 1501420.

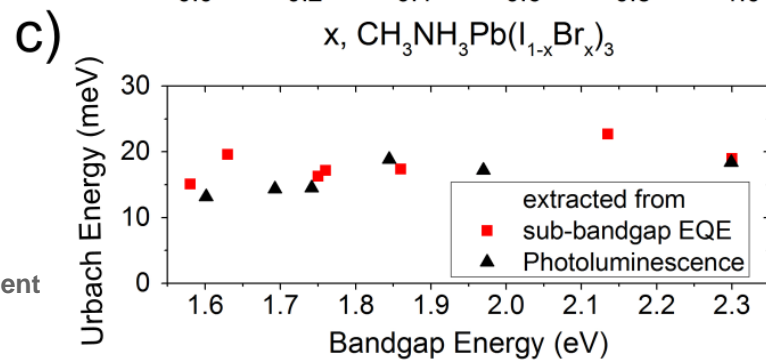
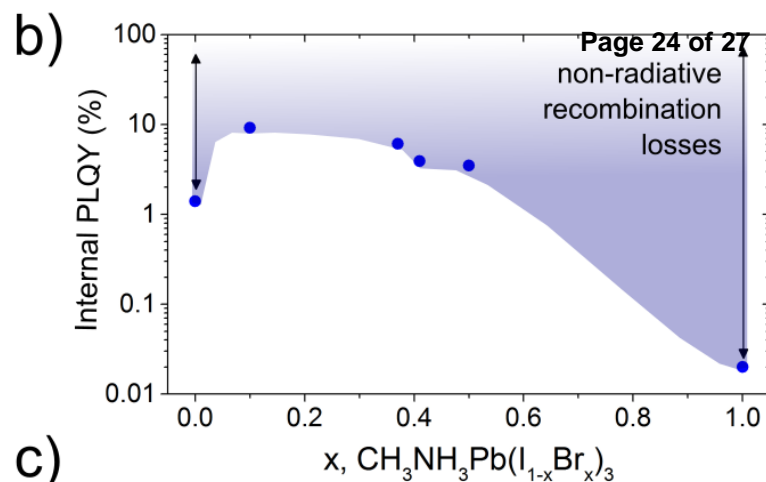
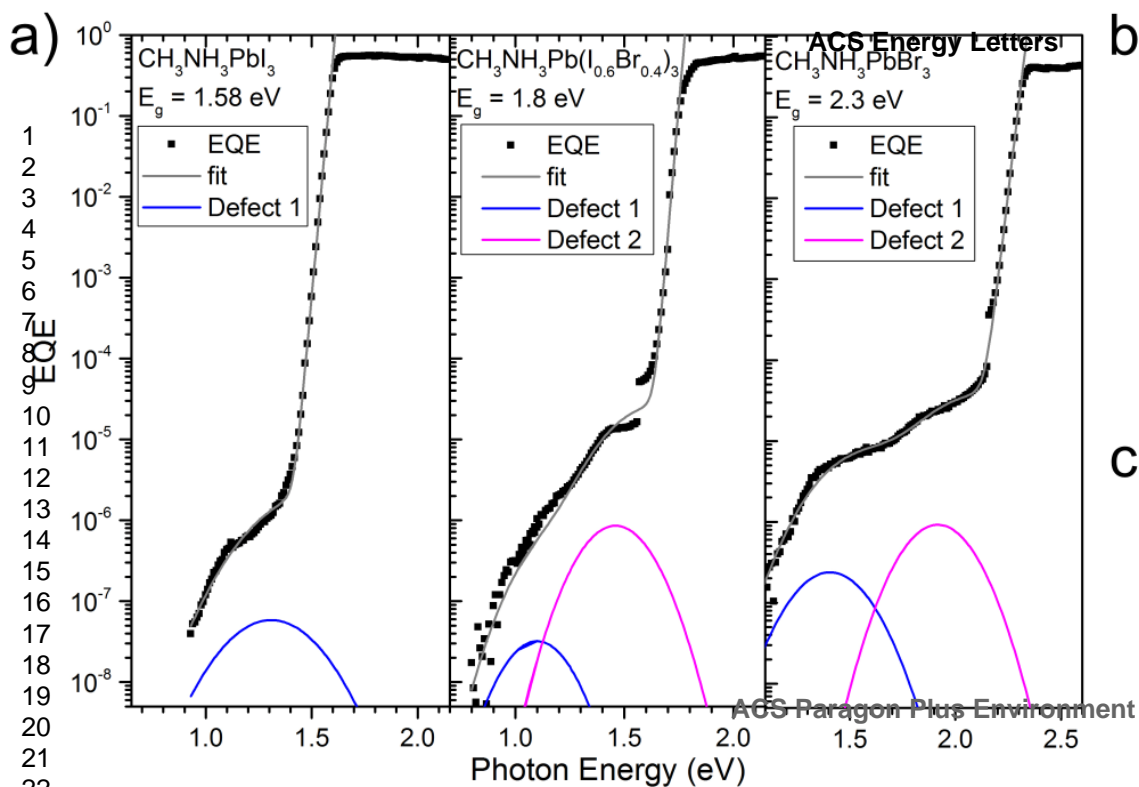
22
23 (38) Chen, Q.; Zhou, H.; Song, T.-B.; Luo, S.; Hong, Z.; Duan, H.-S.; Dou, L.; Liu, Y.; Yang,
24 Y. Controllable Self-Induced Passivation of Hybrid Lead Iodide Perovskites toward High
25 Performance Solar Cells. *Nano Lett.* **2014**, *14*, 4158–4163.

26
27 (39) Jiang, F.; Rong, Y.; Liu, H.; Liu, T.; Mao, L.; Meng, W.; Qin, F.; Jiang, Y.; Luo, B.;
28 Xiong, S. et al. Synergistic Effect of PbI₂ Passivation and Chlorine Inclusion Yielding High
29 Open-Circuit Voltage Exceeding 1.15 V in Both Mesoscopic and Inverted Planar
30 CH₃NH₃PbI₃(Cl)-Based Perovskite Solar Cells. *Adv. Funct. Mater.* **2016**, *26*, 8119–8127.
31
32
33
34
35
36
37
38
39
40
41
42
43
44
45
46
47
48
49
50
51
52
53
54
55
56
57
58
59
60

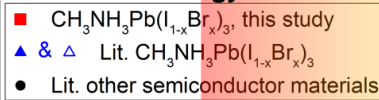


b)





Urbach Energy (meV)



9
10
11
12

ACS Paragon Plus Environment

Bandgap Energy (eV)

